Chapter 3

COMPUTATIONAL PROCEDURE FOR LOWER BOUND FELA WITH NONLINEAR OPTIMIZATION

3.1 INTRODUCTION

This chapter describes the lower bound finite element limit analysis, which can be adopted for solving any axisymmetric geotechnical stability problems. The chapter broadly consists of two sections. The first section exhibits a three-fold demonstration: (a) explaining the development of the constraints and the objective function in the LB-FELA technique, (b) illustrating the smoothening procedure of the yield criteria, and (c) elaborating the step-by-step procedure of the adopted nonlinear optimization technique for computing the lower bound collapse load. In the second section, the bearing capacity factors of pile footing inserted into a non-homogenous cohesive stratum are evaluated by employing the mentioned numerical schema in the first section.

In the first part, an axisymmetric lower bound formulation is presented, by using two-dimensional finite elements, and a three-dimensional yield criterion. In the entire thesis, the three-noded constant strain triangles are used for the sake of discretization of the chosen domain. The reasons for choosing the linear elements lie in their inherent advantages, such as: (a) flexibility of attaining the linear equality constraints, (b) easiness in implementing the stress discontinuities along the interfaces shared by the adjacent elements, and (c) ensuring the yield constraint over an entire element just by satisfying the yield constraints only at the vertices of the element. Four unknown stresses are associated with each node of the triangular element. Stress equilibrium equations are satisfied within the elements and the stress discontinuity conditions are satisfied across the interfaces shared by the adjacent elements. The smoothened form of

the Mohr-Coulomb and Tresca yield surfaces are employed to represent the drained sands and undrained clays, respectively.

In the second part of this chapter, the efficacy of the methodology is verified by computing the bearing capacity factors for pile footing embedded in heterogenous clays. The bearing capacity of pile foundations that are often used to transfer the load of heavy structures to an underlying hard stratum at deeper depths had been obtained earlier with the usage of the (i) limit equilibrium method (Meyerhof, 1963, 1976; Janbu, 1976), (ii) expansion of cavities (Vesic, 1975), (iii) slip line method (Hansen, 1970; De Simone and Sapio, 1985; Houlsby and Martin, 2003), (iv) displacement based elastoplastic finite element/meshfree method (Desai, 1974; Maheshwari et al., 2005), and (v) digital image analysis (Hajialilue-Bonab et al., 2011). By using the axisymmetric finite element lower bound limit analysis, Khatri and Kumar (2009) determined the bearing capacity factor, N_c, for piles embedded in a fully cohesive soil whose cohesion increases linearly with depth. However, the lower bound formulation used by Khatri and Kumar (2009) was based on the implementation of the Von–Karmann hypothesis and the linearized form of the Mohr-Coulomb yield surface. An effort has been made to obtain the bearing capacity factor N_c for an axially loaded pile embedded in clays using the axisymmetric linear two-dimensional finite elements and the three-dimensional smoothened Tresca yield criterion. Failure patterns are also drawn for a few cases, and the obtained solutions are compared with those available in the literature.

3.2 LOWER BOUND LIMIT ANALYSIS FORMULATION

3.2.1 Discretization of domain

The first step of LB–FELA is to discretize the domain with the three nodded linear strain triangular elements (the simplest form of a 2D linear element). Each node of a triangular element is assigned four unknown stress variables (σ_r, σ_z, σ_θ, and τ_{rz}), as

mentioned in shown in Figure 3.1a. The stress components are assumed to vary linearly throughout the element using linear shape functions. Hence, the stresses within an element can be expressed as follows:

$$\sigma_r^e = \sum_{i=1}^{3} N_i^e \sigma_{r,i}^e \; ; \; \sigma_z^e = \sum_{i=1}^{3} N_i^e \sigma_{z,i}^e \; ; \tau_{rz}^e = \sum_{i=1}^{3} N_i^e \tau_{rz,i}^e \; ; \; \sigma_\theta^e = \sum_{i=1}^{3} N_i^e \sigma_{\theta,i}^e \tag{3.1}$$

Here N_i^e, the linear shape function at any arbitrary point (r, z) of e^{th} element is defined as:

$$N_i^e(r,z) = \frac{1}{2A^e}\left[(r_j z_k - r_k z_j) + (z_j - z_k)r + (r_k - r_j)z\right]; \; A^e = 0.5 \left| r_{ik} z_{jk} - r_{kj} z_{ki} \right| \tag{3.2}$$

i, j and k represent the nodes (numbered counter-clockwise) of a triangular element in a r–z plane.

3.2.2 Element equilibrium condition

Considering the statical force equilibrium equations, for an element, e, the spatial gradient of the stress components along the r and z axes can be expressed as below:

$$\left.\frac{\partial \sigma_r}{\partial r} + \frac{\partial \tau_{rz}}{\partial z} + \frac{\sigma_r - \sigma_\theta}{r}\right|^e = 0 \; ; \; \left.\frac{\partial \sigma_z}{\partial z} + \frac{\partial \tau_{rz}}{\partial r} + \frac{\tau_{rz}}{r}\right|^e = \gamma \text{ ; where, } \gamma = \text{soil unit weight} \tag{3.3}$$

Following Sloan (1989), the tensile normal stresses are taken to be positive, as illustrated in Figure 3.1b. These equations are valid at every point of the triangle. The first two terms of the equilibrium equations are the functions of the nodal stresses and the nodal coordinates; therefore, these terms are unique for an element. However, the third component varies spatially because it depends on the stress state and the coordinates of the considered points. Obeying Kumar and Khatri (2011), the expressions of $(\sigma_r - \sigma_\theta)/r$ and τ_{rz}/r for an element, e, are evaluated only at the centroid of that element, as under:

$$\left.\frac{\sigma_r-\sigma_\theta}{r}\right|^e=\frac{\sigma^e_{r,1}+\sigma^e_{r,2}+\sigma^e_{r,3}}{3\bar{r}}-\frac{\sigma^e_{\theta,1}+\sigma^e_{\theta,2}+\sigma^e_{\theta,3}}{3\bar{r}};\quad \left.\frac{\tau_{rz}}{r}\right|^e=\frac{\tau^e_{rz,1}+\tau^e_{rz,2}+\tau^e_{rz,3}}{3\bar{r}} \tag{3.4}$$

Here, $\bar{r}$ refers to the *r*–coordinate at the centroid of the triangle element.

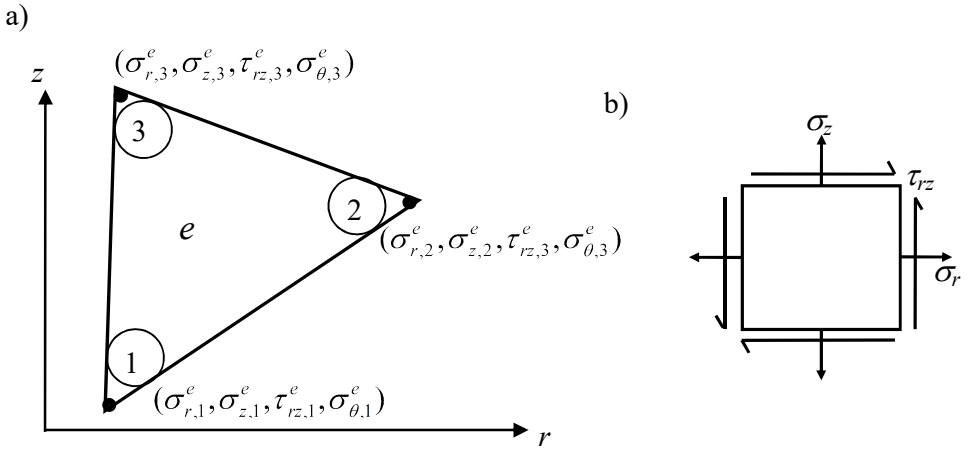

Figure 3.1 a) Pictorial representation of element equilibrium within an element; and b) the sign convention for normal and shear stresses

Implementation of Equation (3.4) indicates that the equilibrium equations are satisfied solely at the centroid of the triangular elements and not throughout the entire domain. The following two equality constraints are generated for any triangular element, *e*, by substituting Equations (3.1), (3.2), and (3.4) into Equation (3.3):

$$\left[a^e_{eq}\right]_{(2\times12)}\left\{\boldsymbol{\sigma}^e\right\}_{(12\times1)}=\left\{\boldsymbol{b}^e_{eq}\right\}_{(2\times1)} \tag{3.5}$$

$$\left[d^e_{eq}\right]=\begin{bmatrix}\frac{z_{23}}{2A^e}+\frac{1}{3\bar{r}} & 0 & \frac{r_{32}}{2A^e} & \frac{-1}{3\bar{r}} & \frac{z_{31}}{2A^e}+\frac{1}{3\bar{r}} & 0 & \frac{r_{13}}{2A^e} & \frac{-1}{3\bar{r}} & \frac{z_{12}}{2A^e}+\frac{1}{3\bar{r}} & 0 & \frac{r_{21}}{2A^e} & \frac{-1}{3\bar{r}}\\ 0 & \frac{r_{32}}{2A^e} & \frac{z_{23}}{2A^e}+\frac{1}{3\bar{r}} & 0 & 0 & \frac{r_{13}}{2A^e} & \frac{z_{31}}{2A^e}+\frac{1}{3\bar{r}} & 0 & 0 & \frac{r_{21}}{2A^e} & \frac{z_{12}}{2A^e}+\frac{1}{3\bar{r}} & 0\end{bmatrix}$$

$$\left\{\boldsymbol{\sigma}^e\right\}^T=\left\{\sigma^e_{r,1}\quad\sigma^e_{z,1}\quad\tau^e_{rz,1}\quad\sigma^e_{\theta,1}\quad\sigma^e_{r,2}\quad\sigma^e_{z,2}\quad\tau^e_{rz,2}\quad\sigma^e_{\theta,2}\quad\sigma^e_{r,3}\quad\sigma^e_{z,3}\quad\tau^e_{rz,3}\quad\sigma^e_{\theta,3}\right\};$$

$$\left\{\boldsymbol{b}^e_{eq}\right\}^T=\left\{0\quad\gamma\right\}$$

3.2.3 Statically admissible stress discontinuity condition

The striking feature of the LB- FELA technique is its ability to accommodate the stress discontinuities along the interfaces of the adjacent elements. According to the stress discontinuity, the tangential stress components (σ_r, σ_z, σ_θ, and τ_{rz}) evaluated at two points, having the same coordinates but associated with two different elements, need not be equal. However, the normal and shear stress along the interface line remains continuous. Mathematically, the condition for imposing the statically admissible stress discontinuity along the interface shared by elements *a* and *b* (as illustrated in Figure 3.2a) can be expressed as follows:

$$\sigma_{n,1}^{a} = \sigma_{n,2}^{b}; \quad \tau_{nt,1}^{a} = \tau_{nt,2}^{b} \quad \text{and} \quad \sigma_{n,3}^{a} = \sigma_{n,4}^{b}; \quad \tau_{nt,3}^{a} = \tau_{nt,4}^{b} \tag{3.6}$$

Notably, the coordinates of nodes 1 and 2 and the coordinates of nodes 3 and 4 are precisely the same.

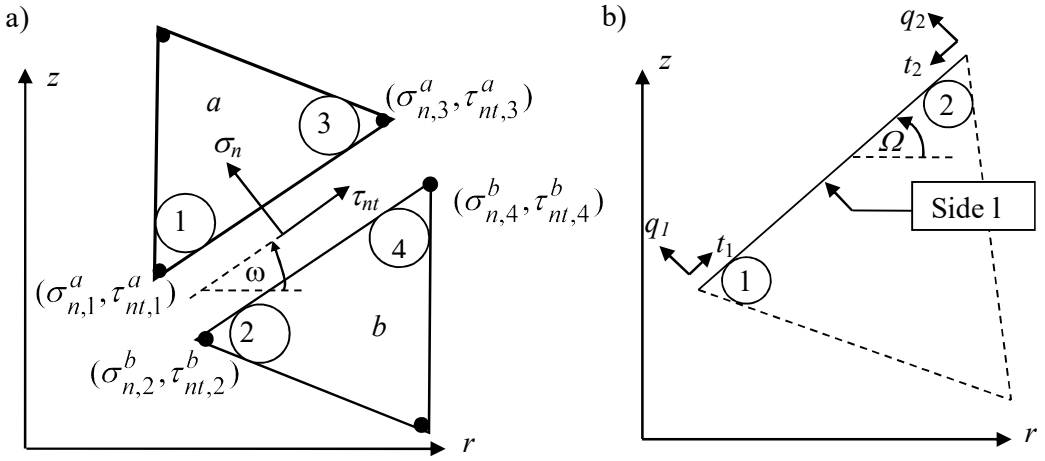

Figure 3.2 a) Stress discontinuity condition along the interface shared by two adjacent elements, *a* and *b*; and b) stress boundary conditions along any edge 1-2.

The expressions of the normal (σ_n) and shear (τ_{nt}) stress acting on a plane that makes an angle ω to the *r*-axis (measured positive anticlockwise) are given by:

$$\sigma_n = \sigma_r \sin^2 \omega + \sigma_z \cos^2 \omega - \tau_{rz} \sin^2 \omega \tag{3.7a}$$

$$\tau_{nt} = -0.5\sigma_r \sin 2\omega + 0.5\sigma_z \sin 2\omega + \tau_{rz} \cos 2\omega \tag{3.7b}$$

Equations (3.6), and (3.7) combinedly generate the following four equality constraints along the interface shared by two nodal pairs (1,2) and (3,4):

$$\left[a_{eq}^{dc}\right]_{(4\times 16)} \left\{\boldsymbol{\sigma}^{dc}\right\}_{(16\times 1)} = \left\{\boldsymbol{b}_{eq}^{dc}\right\}_{(4\times 1)} \tag{3.8}$$

where, $\left[a_{eq}^{dc}\right] = \begin{bmatrix} T & -T & 0 & 0 \\ 0 & 0 & T & -T \end{bmatrix}$; $[T]_{2\times 4)} = \begin{bmatrix} \sin^2\omega & \cos^2\omega & -\sin 2\omega & 0 \\ -0.5\sin 2\omega & 0.5\sin 2\omega & \cos 2\omega & 0 \end{bmatrix}$

$$\left\{\boldsymbol{\sigma}^{dc}\right\}^T = \left\{\sigma_{r,1}^a \;\; \sigma_{z,1}^a \;\; \tau_{rz,1}^a \;\; \sigma_{\theta,1}^a \;\; \sigma_{r,2}^b \;\; \sigma_{z,2}^b \;\; \tau_{rz,2}^b \;\; \sigma_{\theta,2}^b \;\; \sigma_{r,3}^a \;\; \sigma_{z,3}^a \;\; \tau_{rz,3}^a \;\; \sigma_{\theta,3}^a \;\; \sigma_{r,4}^b \;\; \sigma_{z,4}^b \;\; \tau_{rz,4}^b \;\; \sigma_{\theta,4}^b\right\}$$

$$\left\{\boldsymbol{b}_{eq}^{dc}\right\}^T = \{0 \;\; 0 \;\; 0 \;\; 0\}$$

Due to the stress discontinuity constraints, the Mohr circles corresponding to nodal points 1 and 2 are distinct and intersect only at (σ_n , τ_{nt}) points. It can be summarized that, unlike the conventional displacement-based FE method, the Mohr circle (size and location) is not unique to the nodal coordinate.

3.2.4 Stress boundary condition

For a boundary value problem, the prescribed stresses along the domain boundaries must be strictly implemented during the numerical computation. Figure 3.2b shows an arbitrary edge 1–2 (Side *l*) of a domain boundary. The following four equality constraints can express the stress boundary conditions along the given edge:

$$\sigma_{n,1} = q_1 \; ; \quad \tau_{nt,1} = t_1 \quad \text{and} \quad \sigma_{n,2} = q_2 \; ; \quad \tau_{nt,1} = t_2 \tag{3.9}$$

where, q_1, q_2 and t_1, t_1 represent the given normal and shear stresses at nodes 1 and 2, respectively. Similar to Equation (3.7), the normal and shear stresses along the boundary edge can be represented by the tangential stress components at the end nodes and the inclination angle of side l with the horizontal axis. Thus, the equality constraints invoked by a stress boundary edge 1–2 inclined at an angle Ω with the positive r-axis can be rewritten in the following compact form:

$$\left[a_{eq}^{bd}\right]_{(4\times 8)}\left\{\boldsymbol{\sigma}^{bd}\right\}_{(8\times 1)} = \left\{\boldsymbol{b}_{eq}^{bd}\right\}_{(4\times 1)} \tag{3.10}$$

where, $\left[a_{eq}^{bd}\right] = \begin{bmatrix} M & 0 \\ 0 & M \end{bmatrix}$; $\quad \left[M\right]_{(2\times 4)} = \begin{bmatrix} \sin^2\Omega & \cos^2\Omega & -\sin 2\Omega & 0 \\ -0.5\sin 2\Omega & 0.5\sin 2\Omega & \cos 2\Omega & 0 \end{bmatrix}$

$\left\{\boldsymbol{\sigma}^{bd}\right\}^T = \left\{\sigma_{r,1} \quad \sigma_{z,1} \quad \tau_{rz,1} \quad \sigma_{\theta,1} \quad \sigma_{r,1} \quad \sigma_{z,2} \quad \tau_{rz,2} \quad \sigma_{\theta,2}\right\}$; $\left\{\boldsymbol{b}_{eq}^{bd}\right\}^T = \left\{q_1 \quad t_1 \quad q_2 \quad t_2\right\}$

3.2.5 Soil-footing interface condition for a footing problem

The shear stress mobilized below the footing base is characterized by enforcing the following inequality constraints along the soil-footing interface:

$$(c\cot\phi - \sigma_z)\tan\delta \geq -\tau_{rz} \geq 0 \tag{3.11}$$

Here, δ is the roughness angle representing the interface's roughness between the footing and soil. The magnitude of δ ranges between 0° and ϕ. For a perfectly smooth interface, no shear stress is generated (τ_{rz} = 0) along the interface; therefore, δ = 0°. However, when the interface is perfectly rough, shear stress is mobilized up to the soil's shear strength; thus, the perfectly rough condition is realized by equating δ with ϕ. The upper limit of δ arises from the concept that at ultimate shear failure, no point along the footing-soil interface will experience higher mobilized shear stress (τ_{rz}) than the shear strength of the soil mass. During the ultimate shear failure, the shear stress at the

footing-soil interface will act in the opposite direction (as indicated by the sign convention in Figure 3.1b) to resist soil particle movement. While specifying the direction of the shear stress is not necessary, mentioning the correct direction of the mobilized shear stress can save computational time to a considerable extent. The set of inequality constraints at each node of the interface can be written as:

$$h(\boldsymbol{\sigma}) = (-c\cot\phi + \sigma_z)\tan\delta - \tau_{rz} \le 0 \quad \text{and} \quad u(\boldsymbol{\sigma}) = \tau_{rz} \le 0 \tag{3.12}$$

3.2.6 Yield functions

The cohesive-frictional and the purely cohesive soils are modelled with Mohr-Coulomb and the Tresca yield criteria, respectively. The yield criteria can be represented either (a) in terms of the linear yield envelopes represented in the $\sigma_n - \tau_{nt}$ stress space or major (σ_1)–minor (σ_3) principal stress space, or (b) in terms of the yield circles in the ($\sigma_x - \sigma_z$)$-\tau_{xz}$ stress space. Conventionally, the principal stress-based yield functions represent the soil's yield ability during the stability analysis. However, in most cases, especially in axisymmetric problems, which involve one extra dimension of confinement, determining the principal stresses at every domain point becomes a very cumbersome process. To avoid this complexity, following Nayak and Zienkiewicz (1972), the isotropic yield function is reexpressed in the three-dimensional stress invariants (σ_m, $\bar{\sigma}$, θ) space, which constitutes a virtual polar coordinate system and can be denoted as a function of the tangential stress components, as shown below:

$$\sigma_m\,(\text{Hydrostatic Stress}) = \frac{1}{3}(\sigma_r + \sigma_z + \sigma_\theta) \tag{3.13a}$$

$$\bar{\sigma}\,(\text{Octahedral/Deviatoric Stress}) = \sqrt{\frac{1}{2}(s_r^2 + s_z^2 + s_\theta^2) + \tau_{rz}^2} \quad ; \quad s_i = \sigma_i - \sigma_m \quad \left(i = r, z, \theta\right) \tag{3.13b}$$

$$-30^0 \le \theta \text{ (Lode's Angle)} = \frac{1}{3}\sin^{-1}\left(-\frac{3\sqrt{3}}{2}\frac{J_3}{\bar{\sigma}^3}\right) \le 30^0 \;;\; J_3 = s_r s_z s_\theta - s_\theta \tau_{rz}^2 \qquad (3.13c)$$

For isotropic soil, the volumetric (i.e., change in size) and the deviatoric strain (i.e., change in shape) depend on hydrostatic and octahedral stress, respectively. The octahedral stress, $\bar{\sigma}$, refers to the distance between the considered stress state point and the hydrostatic axis in the principal stress space. The Lode angle, θ, indicates the relative magnitude of σ_2 with respect to σ_1 and σ_3. The stress invariants can substitute the principal stresses in the conventional yield criteria by using the following expressions:

$$\sigma_1 = \frac{2}{\sqrt{3}}\bar{\sigma}\sin(\theta + 120^0) + \sigma_m \quad \text{and} \quad \sigma_3 = \frac{2}{\sqrt{3}}\bar{\sigma}\sin(\theta - 120^0) + \sigma_m \qquad (3.14)$$

In compact form, this can be expressed as: $\begin{Bmatrix}\sigma_1\\ \sigma_3\end{Bmatrix} = \sigma_m \begin{Bmatrix}1\\ 1\end{Bmatrix} + \frac{2\bar{\sigma}}{\sqrt{3}}\begin{Bmatrix}\sin(\theta + 120^0\\ \sin(\theta - 120^0\end{Bmatrix}$

The three-dimensional plane in $\sigma_m - \bar{\sigma} - \theta$ space can be viewed in two 2-D planes: the meridian and octahedral planes. The meridian plane represents the relationship between σ_m and θ for a constant $\bar{\sigma}$, whereas the octahedral plane depicts the relationship between $\bar{\sigma}$ and θ at a constant σ_m. The octahedral plane is perpendicular to the hydrostatic axis and is referred to as π-plane or the deviatoric plane. Notably, the hydrostatic axis refers to the axis on which all the principal stresses have the same value, and it makes equal angles with the principal stress axes. The projections of the three principal axes on the octahedral plane, when extended in the negative direction, give rise to six stress sectors. In each of these sectors, the value of θ ranges between 30° and –30°; θ = 30° corresponds to triaxial compression ($\sigma_1 > \sigma_2 = \sigma_3$), and θ = –30° corresponds to triaxial

extension ($\sigma_1 = \sigma_2 > \sigma_3$). The subsequent section elaborates on the form of the MC and the Tresca yield function.

3.2.6.1 Mohr-Coulomb yield function

In terms of the principal stresses the MC yield criterion can be expressed as:

$$f(\boldsymbol{\sigma}) = (\sigma_1 - \sigma_3) + (\sigma_1 + \sigma_3)\sin\phi - 2c\cos\phi \tag{3.15}$$

By using the principal stresses given in Equation (3.14), the yield function in Equation (3.15) can be expressed as:

$$f(\boldsymbol{\sigma}) = \sigma_m \sin\phi + \bar{\sigma}k(\theta) - c\cos\phi = 0 \tag{3.16}$$

where, $k(\theta) = \left(\cos\theta - \frac{1}{\sqrt{3}}\sin\phi\sin\theta \right)$

The MC yield criterion takes the form of a hexagonal pyramid in the 3D principal stress space, as illustrated in Figure 3.3a. The central axis of the pyramid coincides with the hydrostatic axis. The MC yield surface grows continuously with the increase in σ_m; thus, the stress-dependent soil behaviour can be aptly represented by the MC yield criterion. The base of the pyramid is an irregular hexagon, and the apex of the pyramid is positioned on the hydrostatic (space diagonal) axis. Figures 3.3b and 3.3c represents the MC yield surface in the meridian and π-plane, respectively. The size and shape of the yield hexagon on the π-plane are dictated by two parameters, namely, σ_m and ϕ. The shape of the irregular hexagon can be attributed to the fact that the compressive and the tensile strength of the soil are appreciably different. Figure 3.3c clearly shows how the Lode angle will be used to define the stress point in one 60° sector of the π-plane.

3.2.6.2 Tresca yield function

Notably, for completely saturated clays loaded under undrained conditions, the friction angle becomes equal to zero (ϕ_u = 0°). The imposition of zero friction angle eventually converts the MC criterion into the Tresca criterion.

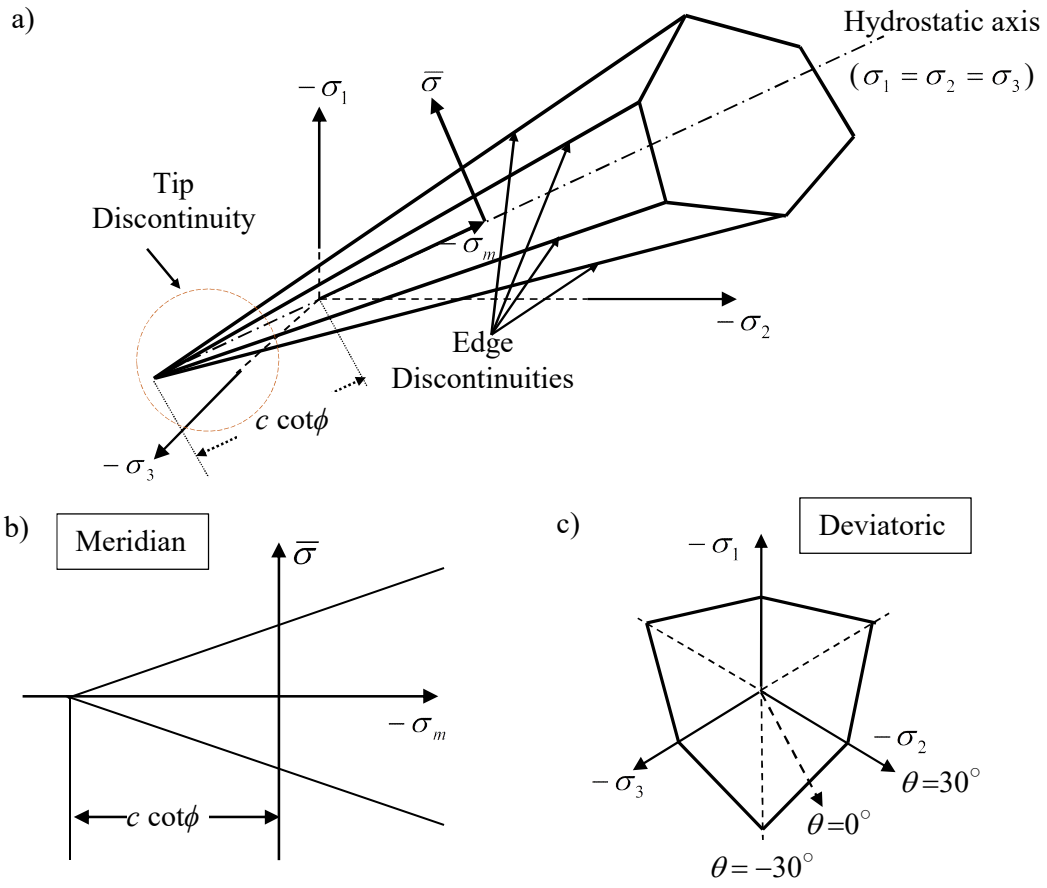

Figure 3.3 a) Original form of Mohr-Coulomb surface in 3-D principal space; (b-c) 2-D planes (meridian and deviatoric).

In terms of the principal stresses, the Tresca yield criterion is expressed as follows:

$$f(\boldsymbol{\sigma}) = (\sigma_1 - \sigma_3) - 2c \tag{3.17}$$

By substituting the principal stresses in terms of stress invariants, the Tresca yield function can be further formulated as follows:

$$f(\boldsymbol{\sigma}) = \overline{\sigma}k(\theta) - c = 0 \quad ; \text{where, } k(\theta) = \cos\theta \tag{3.18}$$

As depicted in Figure 3.4, the Tresca yield surface looks like a hexagonal prism in a 3D principal stress space. The central axis of the prism coincides with the hydrostatic axis. Unlike the MC yield function, the Tresca yield criterion is not dependent on hydrostatic

stress. It is to be noted that the Tresca yield function generates a regular hexagon on the deviatoric plane, and the size of the Tresca hexagon remains to be unique for a specific cohesive strength. Nevertheless, similar to the MC criterion, the Tresca hexagon also possesses sharp corners.

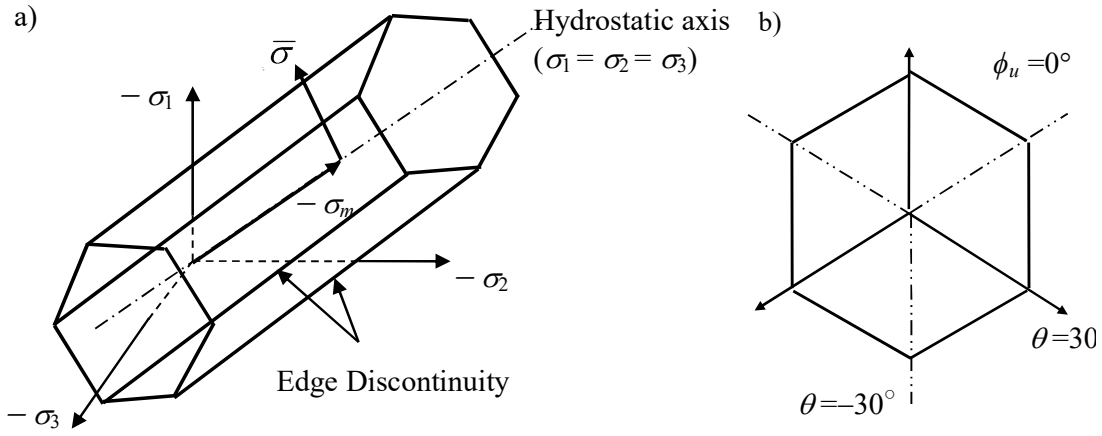

Figure 3.4 a) Tresca yield surface in 3D principal space; and b) Tresca surface in octrahedral plane.

3.2.7 Objective function

In the bearing capacity problem, the basic expression of the objective function is formed by integrating the vertical normal stresses (σ_n) along the surface of the foundation:

$$Q = 2\pi \int_{L_s} \sigma_n r ds \tag{3.19}$$

Here, (i) L_s denotes the length of the boundary surface, s, as shown in Figure 3.5, (ii) r_s represents the distance between the mid-point of the boundary surface and the axis of the footing, (iii) Ψ is the inclination angle of boundary edge, and (iv) the coefficient 2π is associated for taking care of the axisymmetric nature of the problem. Due to the linear variation of the stresses across an element, the contribution of an interface

element onto the collapse load can be written as $Q_{Ls} = 0.5\ L_s(\sigma_{n,1} + \sigma_{n,2})$, where $\sigma_{n,1}$ and $\sigma_{n,2}$ are the normal stresses at nodes 1 and 2, respectively. The normal stresses are again expressed as Equation (3.7). In compact form, Q_{Ls} can be expressed as:

$$Q_{L_s} = \left\{\boldsymbol{g}^s\right\}^T_{(1\times 8)} \left\{\boldsymbol{\sigma}^s\right\}_{(8\times 1)} \tag{3.20}$$

where, $\left\{\boldsymbol{g}^s\right\}^T = \pi L_s r_s \left\{\sin^2\Psi \quad \cos^2\Psi \quad -\sin 2\Psi \quad 0 \quad \sin^2\Psi \quad \cos^2\Psi \quad -\sin 2\Psi \quad 0\right\}$

$$\left\{\boldsymbol{\sigma}^s\right\}^T = \left\{\sigma^s_{r,1} \quad \sigma^s_{z,1} \quad \tau^s_{rz,1} \quad \sigma^s_{\theta,1} \quad \sigma^s_{r,2} \quad \sigma^s_{z,2} \quad \tau^s_{rz,1} \quad \sigma^s_{\theta,2}\right\}$$

Combining the expression of Q_{Ls} along all the interface elements, the global coefficient vector of the objective function can be stated as follows:

$\left\{\boldsymbol{b}\right\} = -\sum_{s=1}^{N_s/2}\left\{\boldsymbol{g}^s\right\}$; where N_s represents the total number of interface elements (3.21)

As tensile normal stresses are treated as positive, −1 is multiplied with $\{\boldsymbol{g}^s\}$.

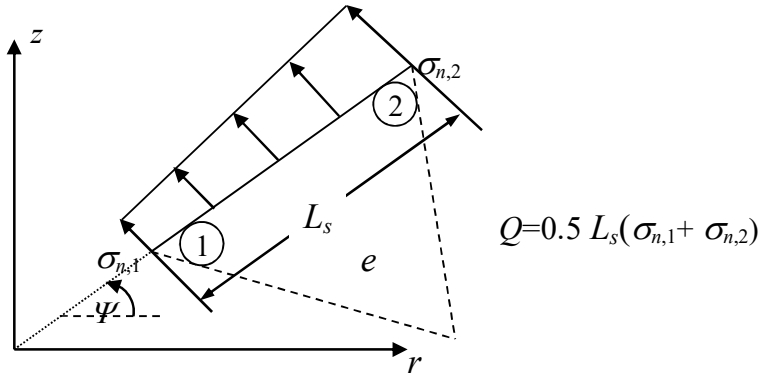

Figure 3.5 Normal stresses acting along any boundary surface, *s*.

3.2.8 Form of the Optimization Problem

After constructing the global equality and non-equality constraints, the canonical form of the optimization problem can be written as:

$$\textit{Maximize} \quad \boldsymbol{b}^T\boldsymbol{\sigma} \tag{3.22a}$$

$$\textit{Subjected to: } \boldsymbol{A_{eq}\sigma = B_{eq}} \text{ and } g(\boldsymbol{\sigma}) \le 0 \tag{3.22b}$$

where, (i) $\boldsymbol{b}$ and $\boldsymbol{\sigma}$ are the global vectors of the objective function (known) and the nodal stresses (unknown), respectively; (ii) $\boldsymbol{A_{eq}}$ and $\boldsymbol{B_{eq}}$ are the coefficient matrix and the right-hand side vector of the equality constraints, respectively; (iii) $\boldsymbol{g}(\boldsymbol{\sigma})$ indicates the global inequalities comprising the nonlinear yield function and the soil-footing interface conditions.

Mathematically, (i) $$\left[\boldsymbol{A}_{eq}\right] = \sum_{e=1}^{E}\left[a_{eq}^{e}\right] + \sum_{dc=1}^{D_c}\left[a_{eq}^{dc}\right] + \sum_{bd=1}^{N_b}\left[a_{eq}^{bd}\right] \tag{3.23a}$$

$$\text{(ii) } \left\{\boldsymbol{B}_{eq}\right\} = \sum_{e=1}^{E}\left\{\boldsymbol{b}_{eq}^{e}\right\} + \sum_{dc=1}^{D_c}\left\{\boldsymbol{b}_{eq}^{dc}\right\} + \sum_{bd=1}^{N_b}\left\{\boldsymbol{b}_{eq}^{bd}\right\} \tag{3.23b}$$

$$\text{(iii) } g(\boldsymbol{\sigma}) = \sum_{j=1}^{N} f_j(\boldsymbol{\sigma}) + \sum_{k=1}^{N_s} h_k(\boldsymbol{\sigma}) + \sum_{l=1}^{N_s} u_l(\boldsymbol{\sigma}) \tag{3.23c}$$

The parameters E, D_c, and N refer to the total number of elements, discontinuities, and nodes. N_s and N_b denote the nodes along the footing–soil interface and the boundary edges where the stresses are defined, respectively. The global vector of unknown nodal stresses $\{\boldsymbol{\sigma}\}$ is expressed as:

$$\{\boldsymbol{\sigma}\}^T = \left[\sigma_{r,1} \quad \sigma_{z,1} \quad \tau_{rz,1} \quad \sigma_{\theta,1} \quad \sigma_{r,2} \quad \sigma_{r,2} \quad \tau_{rz,2} \quad \sigma_{\theta,2} \quad .... \quad ..... \quad \sigma_{r,N} \quad \sigma_{r,N} \quad \tau_{rz,N} \quad \sigma_{\theta,N}\right];$$

3.2.9 Smoothening the yield surfaces

For performing the nonlinear optimization, it becomes necessary to obtain the first and second-order derivatives of the yield function $f(\boldsymbol{\sigma})$. Therefore, the yield surface must be a C^2 continuous surface so that the gradient and Hessian remain unique everywhere in the yield function. It is to be noted that the MC and Tresca criteria, shown in Figues 3.3a and 3.4a, possess sharp discontinuities on the hexagonal vertices in the meridian plane. The vertices of this hexagon form the "edge discontinuities" in the three-dimensional space. Along with the edge discontinuities, the MC yield surface

comprises one more discontinuity, referred to as “tip discontinuity”, at the apex of the pyramid. These discontinuities in the yield geometry create a problem in the numerical computations since the gradient and the Hessian of the yield function would not be unique at those singular points. Following the work of Sloan and Booker (1986) and Abbo et al. (2011), the apex in the meridian plane is smoothened off (using hyperbolic approximation), and the sharp corners in the deviatoric planes are rounded off (using trigonometric approximation) to obtain the C^2 continuous modified smoothened yield surfaces.

3.2.9.1 Smoothening in the meridian plane (for MC surface)

The hyperbolic approximation technique, as proposed by Zienkiewicz & Pande (1977) and Abbo et al. (2011), is utilized to smoothen the tip discontinuity (point P in Figure 3.6) in the meridian plane (i.e., constant θ plane). No matter whatsoever the value of θ is, the yield envelopes in all the $\sigma_m - \overline{\sigma}$ planes pass through the same apex point. Hence, the smoothening operation for the removal of tip discontinuity can be carried out in any meridian plane, regardless of the θ–value. The striking feature of the hyperbolic approximation is that the smoothened surface approaches the original MC yield surface asymptotically as σ_m increases. The hyperbolic approximation gets implemented and controlled solely by one parameter, ε, which physically represents the distance between the tip of the original MC pyramid and the smoothened yield surface along the hydrostatic axis. The quantity, ε, is used to model the original yield surface as accurately as desired by relating ε with the material strength parameters as $\varepsilon = \kappa c\cot\phi$; the value of κ ranges from 0 to 1 (Zienkiewicz & Pande, 1977). In the present thesis, κ is set to 0.05 in all cases. Figures3.6 and 3.7b illustrate the effect of κ on the modified

yield surface's shape in the meridian plane and π-plane, respectively. The magnitude of ε equals zero and infinity for purely cohesionless (c = 0) and perfectly cohesive soil

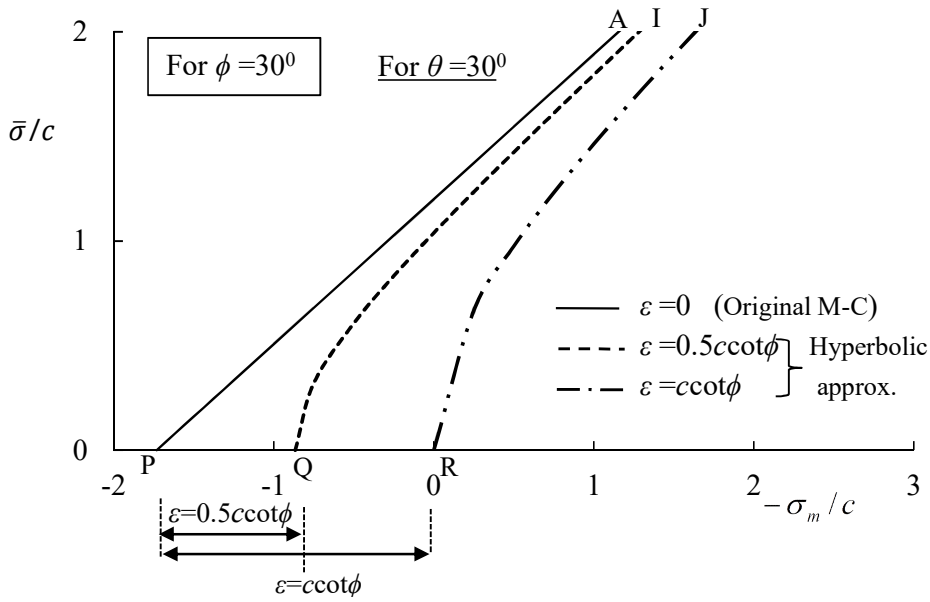

Figure 3.6 Smooth hyperbolic approximation of MC yield surface in meridian section.

(ϕ = 0°), respectively. And this creates a problem in the numerical computation. To avoid such a problem, the minimum threshold values of (i) $c_{\min}$ =10^{-3} kPa, and (ii) $\phi_{\min}$ =10^{-3} radians are chosen.

3.2.9.2 Smoothening in the deviatoric plane (for MC and Tresca surfaces)

An exercise is performed for smoothening off the six sharp corners of the irregular (MC criterion) and regular (Tresca criterion) hexagon in the deviatoric plane. This smoothening exercise is done by rounding off the yield surface near the sharp corners using trigonometric approximations. In each sector (−30° ≤ θ ≤ 30°), two transition Lode angles are to be chosen close to the singular point. Nevertheless, to simplify the numerical procedure, the transition angle is chosen to be the same near the compression and extension vertices. Symbolically, the transition angle is denoted as θ_T.

Upto θ_T, the yield criterion is governed by the original yield surface. Beyond that, the yield surface moves from the parent yield surface to the modified yield surface, formulated as a trigonometric function. At the transition point, the following three criteria are enforced to establish smooth connectivity between the original and the modified yield criteria:

(i) $\bar{\sigma}$ invariant for the modified yield surface = $\bar{\sigma}$ invariant for the original MC surface

(ii) $\frac{\partial\bar{\sigma}}{\partial\theta}$ invariant for the modified yield surface = $\frac{\partial\bar{\sigma}}{\partial\theta}$ invariant for the original MC surface

(iii) $\frac{\partial^2\bar{\sigma}}{\partial\theta^2}$ invariant for the modified yield surface = $\frac{\partial^2\bar{\sigma}}{\partial\theta^2}$ invariant for the original MC surface

(iv) $\frac{\partial\bar{\sigma}}{\partial\theta}$ obtained at $\theta = \pm 30°$ must be equal to zero.

The equation of the modified yield surface is derived by satisfying the three conditions mentioned above at the transition point, $|\theta| = \theta_T$. Furthermore, the gradient of $\bar{\sigma}$ at $\theta = \pm 30°$ must be equal to zero. Based on these conditions, the parameter $k(\theta)$ is redefined. The redefinition of $k(\theta)$ plays a significant role in transforming the parent yield surface into a C^2 continuous modified smoothened yield in the vicinity of the sharp corners of the parent hexagon.

Smoothened form of the yield surfaces

By using the offset distance, ε, and the transition Lode angle, θ_T, the complete form of the smoothened yield criteria are expressed as follows:

Smoothened MC criterion: $f(\boldsymbol{\sigma}) = \sigma_m \sin\phi + \sqrt{\bar{\sigma}^2 k(\theta)^2 + \varepsilon^2 \sin^2\phi} - c\cos\phi$ (3.24)

Smoothened Tresca Criterion: $f(\boldsymbol{\sigma}) = \bar{\sigma}k(\theta) - c$ (3.25)

Smoothened Mohr-Coulomb Yield Criterion

$$k(\theta) = \left(\cos\theta - \frac{1}{\sqrt{3}} \sin\phi \sin\theta \right) \quad for \ |\theta| \le \theta_T$$

$$= \left(A + B\sin 3\theta + C\sin^2 3\theta \right) \quad for \ |\theta| > \theta_T$$

$$A = -\langle\theta\rangle \sin\phi \sin\theta_T / \sqrt{3} - B\langle\theta\rangle \sin 3\theta_T - C\sin^2 3\theta_T + \cos\theta_T \ ;$$

$$B = \langle\theta\rangle M_1 \sin 6\theta_T - 6M_2 \cos 6\theta_T / M_3 \ ;$$

$$C = -M_1 \cos 3\theta_T - 3M_2 \langle\theta\rangle \sin 3\theta_T / M_3 ;$$

$$M_1 = \cos\theta_T - \langle\theta\rangle \sin\phi \sin\theta_T / \sqrt{3} \ ;$$

$$M_2 = \langle\theta\rangle \sin\theta_T + \sin\phi \cos\theta_T / \sqrt{3} \ ;$$

$$M_3 = 18\cos^3 3\theta_T$$

Smoothened Tresca Yield Criterion
(By placing ϕ=0° in MC yield criterion)

$$k(\theta) = \cos\theta \quad for \ |\theta| \le \theta_T$$

$$= \left(A + B\sin 3\theta + C\sin^2 3\theta \right) \ for \ |\theta| > \theta_T$$

$$A = -B\langle\theta\rangle \sin 3\theta_T - C\sin^2 3\theta_T + \cos\theta_T$$

$$B = \langle\theta\rangle M_1 \sin 6\theta_T - 6M_2 \cos 6\theta_T / M_3 \ ;$$

$$C = -M_1 \cos 3\theta_T - 3M_2 \langle\theta\rangle \sin 3\theta_T / M_3 ;$$

$$M_1 = \cos\theta_T ; M_2 = \langle\theta\rangle \sin\theta_T \ ; M_3 = 18\cos^3 3\theta_T$$

$$\langle\theta\rangle = 1 \quad \text{if } \theta \ge 0^0$$

$$= -1 \quad \text{elsewise}$$

The two control parameters, ε and θ_T (transition angle), eliminate all the sharp discontinuities from the meridian and octahedral planes, respectively. Figure 3.7 illustrates how the segments MD and NE in the original MC yield surface are smoothened near the sharp vertices D and E. Notably, θ_T is the sole controlling parameter that smoothens the Tresca yield surface in the three-dimensional stress space. While selecting the value of θ_T, there is a trade-off between the ill-conditioning of the coefficients A, B and C and the accuracy of the estimated bearing capacity factor (Taiebat and Carter, 2008). The accuracy of the solution, particularly for an axisymmetric case (Abbo et al., 2011), improves as θ_T approaches 30°. On the contrary, the expression of $k(\theta)$ becomes ill-conditioned when θ_T is very close to 30° (Sloan and Booker, 1986; Taiebat and Carter, 2008). In the present analysis, the magnitudes of ε and θ_T are taken as $0.05c\cot\phi$ and 29.50°, respectively. The original yield surface will be retained by placing $\varepsilon = 0$ and $\theta_T = 30°$.

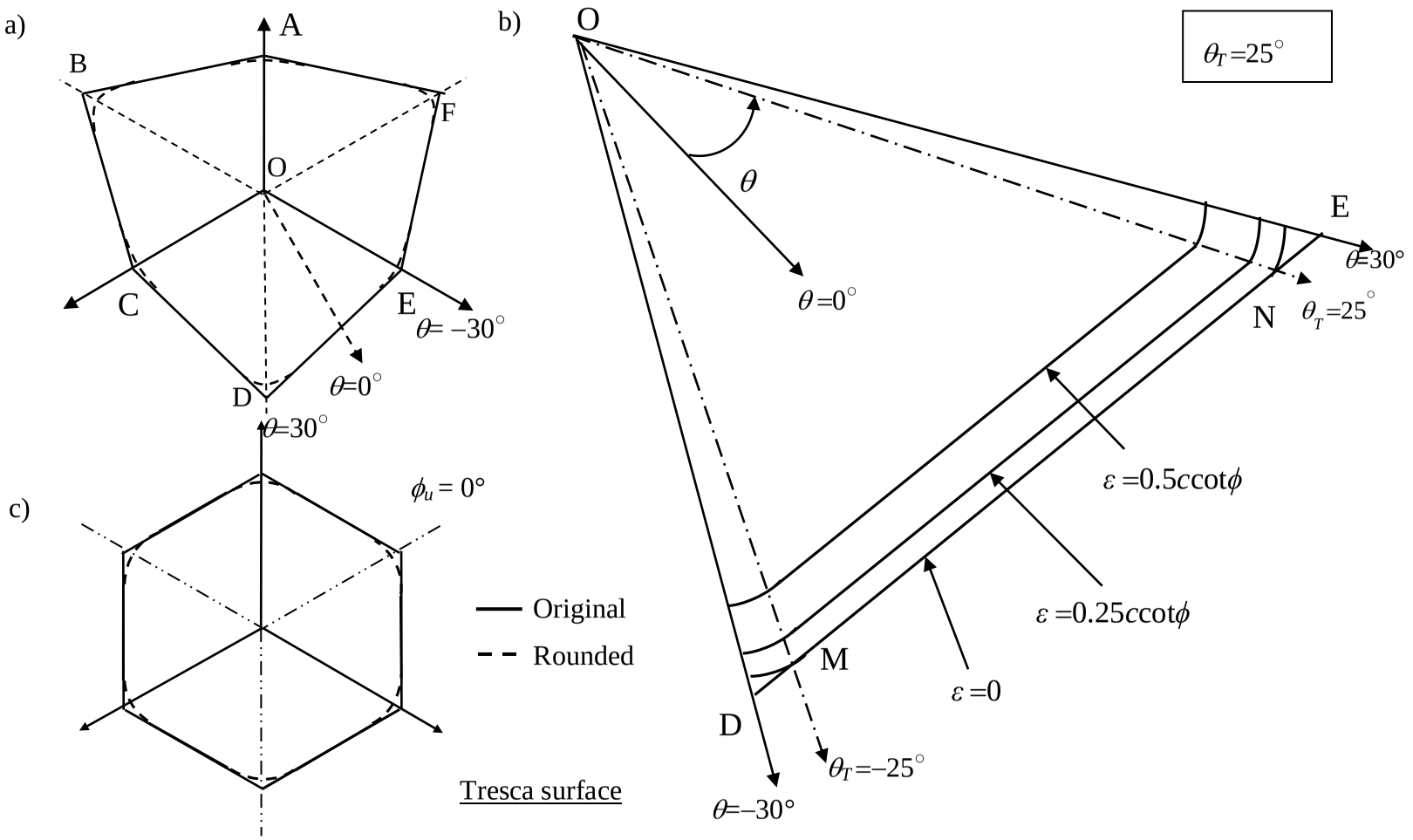

Figure 3.7 Mohr-Coulomb yield surface in a π-plane a) with sharp vertices; b) rounded hyperbolic form (C^2–continuity) of one side of the hexagon; and c) complete rounded surface for ϕ = 0 (Tresca) case.

3.2.10 Procedure

The lower bound problem stated in Equation (3.22) is solved by adding a logarithmic barrier function to the objective function and performing the optimization by using the interior-point method (IPM). The IPM's algorithm simultaneously solves the primal and dual programs by reducing the duality gap during each iteration. The optimization problem is reexpressed as follows:

$$\text{Maximize: } \boldsymbol{b}^T\boldsymbol{\sigma} + \mu^k \sum_{j=1}^{(N+2N_s)} \log s_j \tag{3.26}$$

$$\text{Subject to : } \boldsymbol{A}_{eq}\boldsymbol{\sigma} = \boldsymbol{B}_{eq} \quad \text{and} \quad g(\boldsymbol{\sigma}) + \boldsymbol{s} = \boldsymbol{0} \tag{3.27}$$

where, (i) μ^k is a barrier parameter at k^{th} iteration; (ii) $\boldsymbol{s}$ is the complementary slack variable; (iii) $\boldsymbol{A}_{eq}$ and $\boldsymbol{B}_{eq}$ are the coefficient matrix and the right-hand side vector of the equality constraints, respectively; (iv) N and N_s are the numbers of total nodes in the soil domain and the surface nodes, respectively. The slack variables are added with the inequality constraints to form the equality constraints.

The Lagrangian polynomial for the present problem can be written as follows:

$$L(\boldsymbol{\sigma}, \boldsymbol{s}, \boldsymbol{\lambda}, \boldsymbol{\upsilon}) = \boldsymbol{b}^T\boldsymbol{\sigma} + \mu^k \sum_{j=1}^{(N+2N_s)} \log s_j - \boldsymbol{\lambda}^T(g(\boldsymbol{\sigma}) + \boldsymbol{s}) - \boldsymbol{\upsilon}^T(\boldsymbol{B}_{eq} - \boldsymbol{A}_{eq}\boldsymbol{\sigma}) \tag{3.28}$$

where, $\boldsymbol{\lambda}$ and $\boldsymbol{\upsilon}$ are the Lagrangian multiplier for the inequality and equality constraints, respectively. The dimension of $\boldsymbol{\lambda}$ and $\boldsymbol{\upsilon}$ precisely align with the combined count of their corresponding constraints.

By employing the Karush-Kuhn-Tucker (KKT) optimality conditions, the Lagrangian polynomial function (L) is made to be stationary with respect to the unknown variables $(\boldsymbol{\sigma}, \boldsymbol{s}, \boldsymbol{\lambda}, \boldsymbol{\upsilon})$. The KKT gradient and the feasibility conditions are stated below:

$$\nabla L(\boldsymbol{\sigma}, \boldsymbol{s}, \boldsymbol{\lambda}, \boldsymbol{\upsilon}) = \begin{bmatrix} \mathbf{r}_{1_{(n,1)}} \\ \mathbf{r}_{2_{(N+2Ns,1)}} \\ \mathbf{r}_{3_{(N+2Ns,1)}} \\ \mathbf{r}_{4_{(m,1)}} \end{bmatrix} = \begin{bmatrix} \nabla g(\boldsymbol{\sigma})\boldsymbol{\lambda} - \boldsymbol{A_{eq}}^T \boldsymbol{\upsilon} - \boldsymbol{b} \\ \boldsymbol{S\lambda} - \mu^k \boldsymbol{e} \\ g(\boldsymbol{\sigma}) + \boldsymbol{s} \\ \boldsymbol{B_{eq}} - \boldsymbol{A_{eq}}\boldsymbol{\sigma} \end{bmatrix} = \begin{bmatrix} \mathbf{0}_{(n,1)} \\ \mathbf{0}_{(N+2Ns,1)} \\ \mathbf{0}_{(N+2Ns,1)} \\ \mathbf{0}_{(m,1)} \end{bmatrix}; \quad \begin{matrix} \boldsymbol{s} \geq \mathbf{0} \\ \boldsymbol{\lambda} \geq \mathbf{0} \\ \boldsymbol{\upsilon} \text{ unrestricted} \end{matrix} \tag{3.29}$$

Here,

(a) $\boldsymbol{e}$ indicates the vector of ones with order ((N+2) × 1) and $\boldsymbol{S}$=diag($\boldsymbol{s}$).

(b) $\mathbf{r_1}$ is the residual associated with the dual feasibility: $\nabla g(\boldsymbol{\sigma})\boldsymbol{\lambda} - \boldsymbol{A_{eq}}^T \boldsymbol{\upsilon} - \boldsymbol{b} = \mathbf{0}$

$\mathbf{r_2}$ is the residual associated with the complementarity equation: $\boldsymbol{S\lambda} = \mathbf{0}$

$\mathbf{r_3}$ is the residual associated with the (inequality) primal feasibility: $g(\boldsymbol{\sigma}) + \boldsymbol{s} = \mathbf{0}$

$\mathbf{r_4}$ is the residual associated with the (inequality) primal feasibility: $\boldsymbol{B_{eq}} - \boldsymbol{A_{eq}}\boldsymbol{\sigma} = \mathbf{0}$

Non-negativity of the slack variables ($\boldsymbol{s} \geq 0$) ensures the feasibility of the inequalities, i.e., $g(\boldsymbol{\sigma}) \leq 0$. It is to be noted that if the stress state of a point lies on the yield surface, the corresponding Lagrange multiplier ($\boldsymbol{\lambda}$) becomes positive, and if the stress state is in the elastic regime, the magnitude of $\boldsymbol{\lambda}$ remains zero. However, the components of the $\boldsymbol{\upsilon}$–vector are free in sign.

The perturbation in the complementarity equations, characterized by the barrier parameter μ^k, is crucial while formulating the IPM algorithm. A heuristic rule (Krabbenhoft and Damkilde, 2003) is applied to update the μ^k parameter at each iteration. During each iteration, the μ^k parameter reduces and approaches zero. This is how the complementarity condition is satisfied, thereby making the duality gap zero and achieving the optimum point. In this process, the log-barrier added objective function traces the central path approximately (Lesaja, 2009) to obtain the global convergence. The stated optimization problem is a convex optimization problem because the

objective function, equality, and interface inequality constraints are linear, and the nonlinear yield criterion is a convex function. Therefore, the global optimum is the same as the local optimum.

The first step involved in the optimization technique is to find a desirable search direction in the design space by using Modified Newton's method. The following sets of simultaneous linear equations are solved to get the direction of the unknown variable vector, $\boldsymbol{d}_x$:

$$\nabla^2 L(\boldsymbol{\sigma}, \boldsymbol{s}, \boldsymbol{\lambda}, \boldsymbol{\upsilon})\, \boldsymbol{d}_x = -\nabla L = -\mathbf{r} \tag{3.30}$$

where, $\boldsymbol{d}_x = \left\{\Delta\boldsymbol{\sigma}_{(n\times 1)} \quad \Delta\boldsymbol{s}_{(N+4t,1)} \quad \Delta\boldsymbol{\lambda}_{(N+4t,1)} \quad \Delta\boldsymbol{\upsilon}_{(l\times 1)}\right\}^T$ and

$$\nabla^2 L = \begin{bmatrix} \boldsymbol{H}_{(n,n)} & \mathbf{0}_{(n,N+4t)} & \nabla g(\boldsymbol{\sigma})_{(n,N+4t)} & -\boldsymbol{A}_{eq}{}^{T}_{(n,m)} \\ \mathbf{0}_{(N+4t,n)} & \boldsymbol{\Lambda}_{(N+4t,N+4t)} & \boldsymbol{S}_{(N+4t,N+4t)} & \mathbf{0}_{(N+4t,m)} \\ \nabla g(\boldsymbol{\sigma})^T_{(N+4t,n)} & \boldsymbol{I}_{(N+4t,N+4t)} & \mathbf{0}_{(N+4t,N+4t)} & \mathbf{0}_{(N+4t,m)} \\ -\boldsymbol{A}_{eq(m,n)} & \mathbf{0}_{(m,N+4t)} & \mathbf{0}_{(m,N+4t)} & \mathbf{0}_{(m,m)} \end{bmatrix}$$

Here, $\mathbf{I}$ = unit matrix, $\boldsymbol{\Lambda}$ = diag ($\boldsymbol{\lambda}$) and $\boldsymbol{H} = \sum_{j=1}^{n} \nabla^2 f_j(\boldsymbol{\sigma})$.

After obtaining the search direction ($\boldsymbol{d}_x$), the step length is computed along the search direction and the unknown variables are updated accordingly. The detailed methodology is elaborated in Appendix A. The implementation of this procedure requires computing the gradient and Hessian matrix of the inequality constraints $g(\boldsymbol{\sigma})$, which includes $h(\boldsymbol{\sigma})$, $u(\boldsymbol{\sigma})$, and $f(\boldsymbol{\sigma})$. The functions $h(\boldsymbol{\sigma})$ and $u(\boldsymbol{\sigma})$ are linear; hence, their gradient is not dependent on the stress state, and all the terms in their Hessian matrix are simply zero. The gradient and the Hessian of the modified smoothened MC and Tresca yield functions, pertaining to the present axisymmetric problem, are presented in Appendix B and Appendix C, respectively.

3.3 NUMERICAL EXAMPLE- ULTIMATE BEARING CAPACITY FACTORS FOR PILE FOOTING EMBEDDED INTO A NON-HOMOGENOUS CLAYEY SOIL

3.3.1 Problem definition

A pile of diameter, B, and length, H, is embedded in clay whose undrained shear strength increases linearly with depth through the following expression:

$$c_u(z) = c_{u0} + \frac{mc_{u0}|z|}{B} \tag{3.31}$$

where, $c_u(z)$ and c_{u0} are the undrained cohesion value at a depth z and at ground surface (as shown in Figure 3.8), respectively, and m is a non-dimensional factor that defines the rate at which cohesion increases with depth. Note that undrained cohesion indicate the intercept of the MC yield envelope on the shear stress axis when the shearing of the soil is carried out under undrained conditions for a given initial stress state. Bishop (1966) had earlier observed this trend of linear increment of cohesion by conducting experimental studies on normally consolidated and lightly overconsolidated saturated clays under undrained conditions. The pile is subjected to a vertical compressive downward load of magnitude Q_u which acts at the centre of the pile without any eccentricity. The soil medium is considered to be perfectly plastic and obeys the normality rule of flow condition. It is required to determine the lower bound bearing capacity factor N_c for different combinations of m and H/B (embedment ratio) corresponding to different roughness conditions of the pile shaft and the pile base; here, H and B indicate the height and the diameter of the circular pile. Assuming the superposition theorem is valid, the bearing capacity factor N_c is computed by considering the soil mass to be ponderless with zero surcharging.

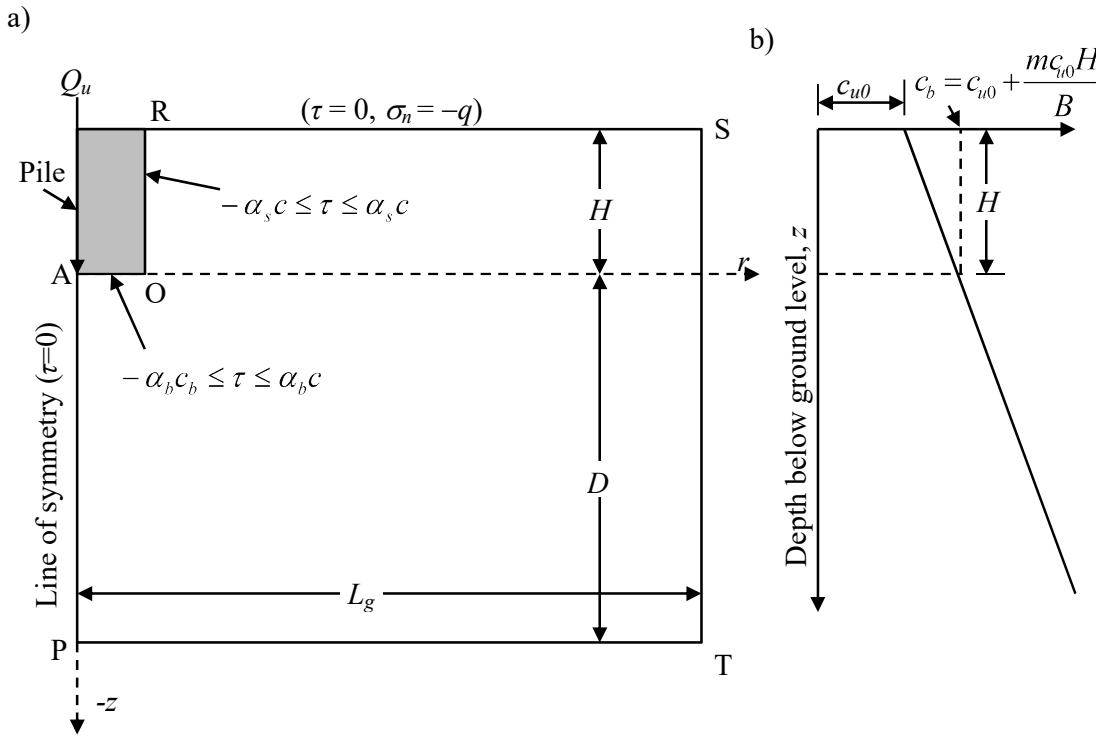

Figure 3.8 a) Problem domain and associated boundary conditions, b) variation of cohesion within the soil domain.

3.3.2 Problem domain, boundary conditions and mesh details

Considering the fact that the domain is symmetric about the axis of the pile, only one-half of the total domain in an *r*-*z* plane is employed. The domain and the associated stress boundary conditions are shown in Figure 3.8a. The values of L_g and D were taken sufficiently large so that the plastic zones generated from the analysis must be contained well within the domain, and the obtained N_c value does not get changed even if the domain size is increased further. In the present analysis, L_g and D were kept equal to 9B and 7B, respectively.

Along the centre line (AP) of the pile and along the ground surface (RS), the shear stress is kept equal to zero. In this analysis, only the magnitude of the bearing load is evaluated based on the pile-base resistance; the total load, which will also include the shaft resistance, has not been considered. For satisfying roughness conditions along the

soil-pile base interface (AO) and along soil–pile shaft interface (RO), the following conditions are imposed:

$$|\tau_{rz}| \leq \alpha_b c_b \text{ and } |\tau_{rz}| \leq \alpha_s c; \tag{3.32}$$

where, α_b and α_s represent the adhesion factor for cohesion along the pile base (c_b) and along the pile shaft–soil interface, respectively. The values of adhesion factors are kept equal to 0 and 1 for perfectly smooth and perfectly rough bases, respectively. The value of soil cohesion at the level of pile base is denoted by c_b (as shown in Figure 3.8). Moreover, σ_r and σ_z along the soil-pile shaft interface are considered to be zero as the soil mass is assumed to be weightless. Three-nodded triangular elements were used to model the stress domain in the *r-z* plane. The mesh (as shown in Figure 3.9) was drawn in such a fashion that the sizes of the elements gradually become smaller when approaching the periphery of the pile base.

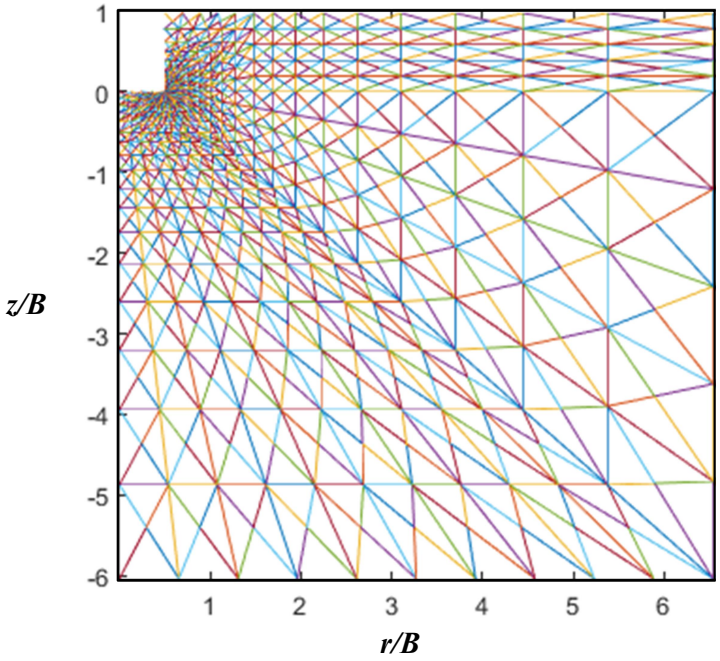

Figure 3.9 Finite Element meshes for $\alpha_b = 1$, $\alpha_s = 1$.

3.3.3 Results and Discussion

3.3.3.1 Numerical solutions

The computations were performed for different values of *H/B* ranging from 0 to 4 and *m* varying from 0 to 5. Figure 3.10 depicts that the value of N_c increases with the increase of *m* and *H/B*. For any *H/B*, the rate of increment of N_c is quite higher in the lower range of *m*. The increment of N_c with *H/B* diminishes as the length of the pile increases. The N_c value for *H/B* = 1 and 2 are almost the same. For *H/B* = 1, the variation of N_c with respect to *m* for different roughness condition of soil-pile base interface and soil-pile shaft interface is presented in Figure 3.11. It is well observed that the roughness condition enhances the bearing capacity factor. Moreover, in comparison to the pile base, roughness along pile shaft plays crucial role in enhancing the bearing load. In all the cases, it is observed that upto a certain *m* value N_c increases; beyond that, the value of N_c remains to be constant.

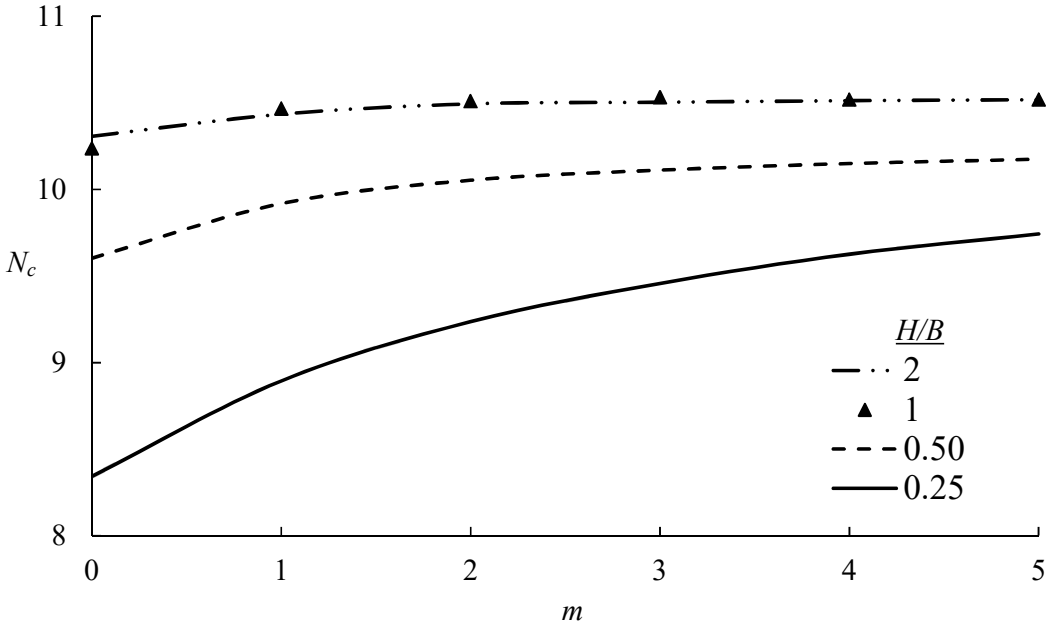

Figure 3.10 The variation of N_c with respect to *m* for different *H/B* ratio of pile for $\alpha_b = 1$, $\alpha_s = 1$

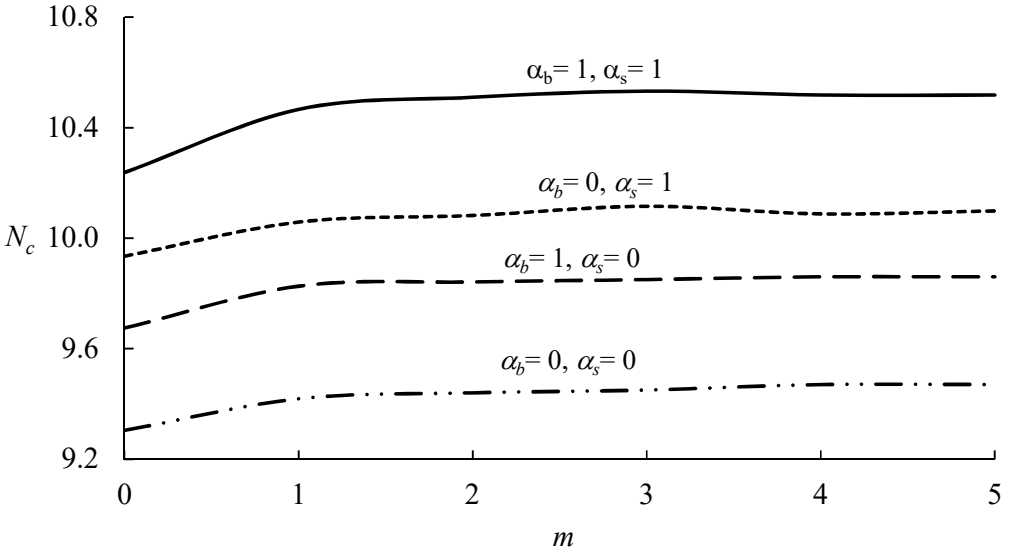

Figure 3.11 The variation of N_c with respect to m for different roughness condition at the pile base and pile shaft

3.3.3.2 Failure patterns

After the lower bound limiting state is attained, the failure patterns are drawn by using the stress components (σ_r, σ_z, σ_θ, and τ_{rz}) obtained at each node. By using the stress components, the principal stresses σ_1 and σ_3 at each node are obtained by employing the following expressions:

$$\sigma_1, \sigma_3 = \frac{\sigma_r + \sigma_z}{2} \pm \sqrt{\left(\frac{\sigma_r - \sigma_z}{2}\right)^2 + \tau_{rz}^2} \tag{3.33}$$

The proximity of a point to shear failure can be computed by evaluating the *a/d* ratio through the following expressions:

$$a = \left(\frac{\sigma_{\max} - \sigma_{\min}}{2}\right)^2 + \tau^2; \quad \text{if}, \sigma_{\max} \geq \sigma_\theta \geq \sigma_{\min}, \ \tau = \tau_{rz} \text{ or else } \tau = 0 \tag{3.34}$$

Here, σ_{max} = max [σ_1, σ_3, σ_θ] and σ_{min} = min [σ_1, σ_3, σ_θ]. As the present case is a purely undrained one, hence, the radius of the Mohr circle (d) touching the failure envelope will be equal to cohesion value (c) at that point. The meaning of a and d are illustrated

in Figure 3.12. The point for which a/d = 1 will be in a state of shear failure and is indicated with red colour in the failure contour, and if a/d< 1, the stress state of that point will be non-plastic.

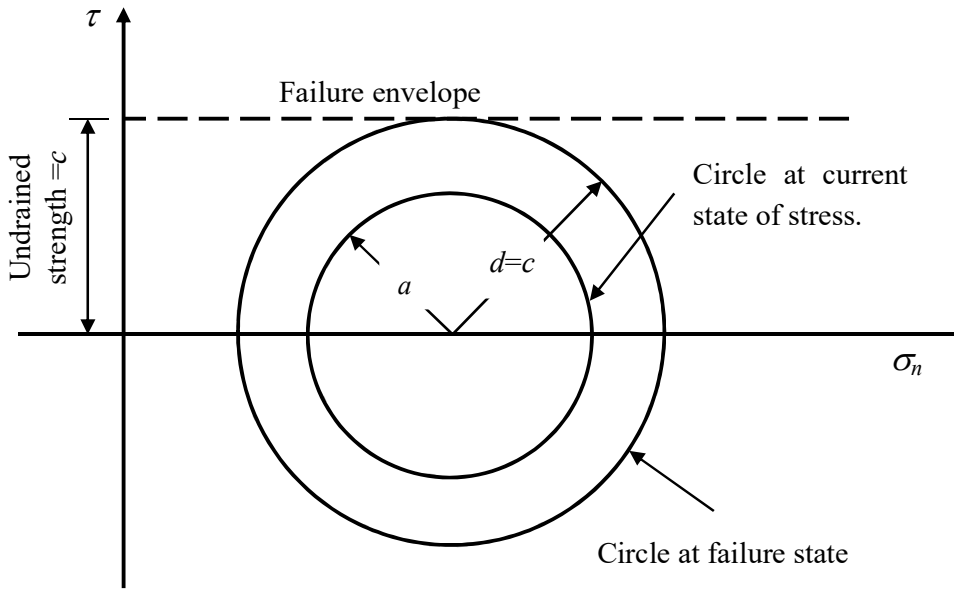

Figure 3.12 Schematic diagram of Mohr's stress circle at failure and current stress state for any arbitrary point in the domain.

Figure 3.13 displays the failure pattern for a foundation for which H/B = 1 and roughness is mobilized along the pile base only. The figure depicts failure pattern for two different cases: (a) m = 0, and (b) m = 4. The extension of the failure zone seems to be more for the second soil. Figures 3.14a and 3.14b provide the failure pattern for two different H/B ratios. The horizontal extent of the plastic domain is more for the higher H/B ratio. Figures 3.14b and 3.14c infer that in contrast to the rough shaft, where the plastic domain extends continuously up to the pile shaft, the failure zone for the smooth shaft diminishes within the soil before reaching the pile shaft.

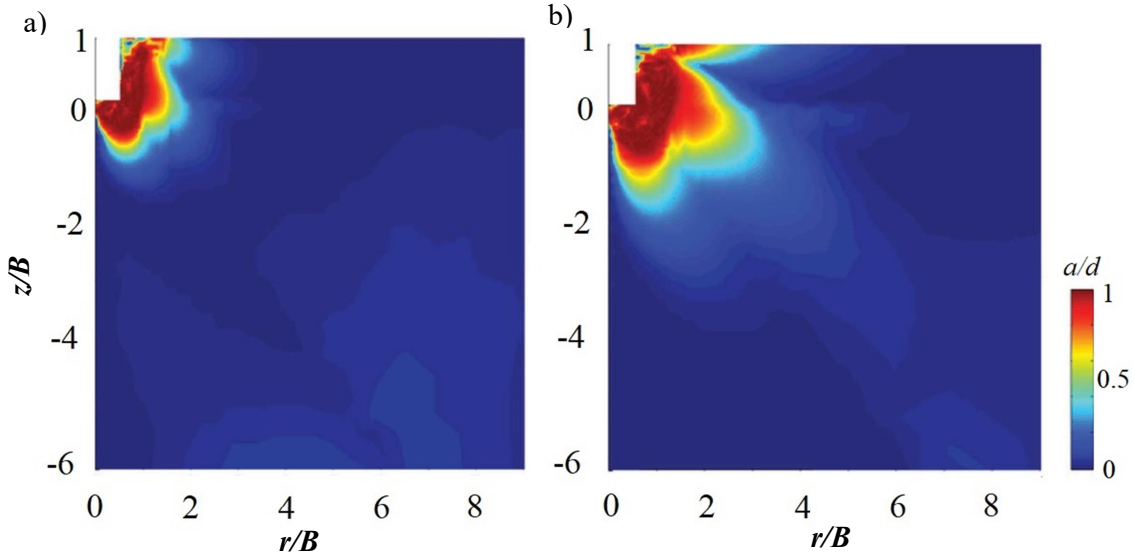

Figure 3.13 Failure pattern for $H/B = 1$ with $\alpha_b = 1$, $\alpha_s = 0$ and a) $m = 0$; and b) $m = 4$.

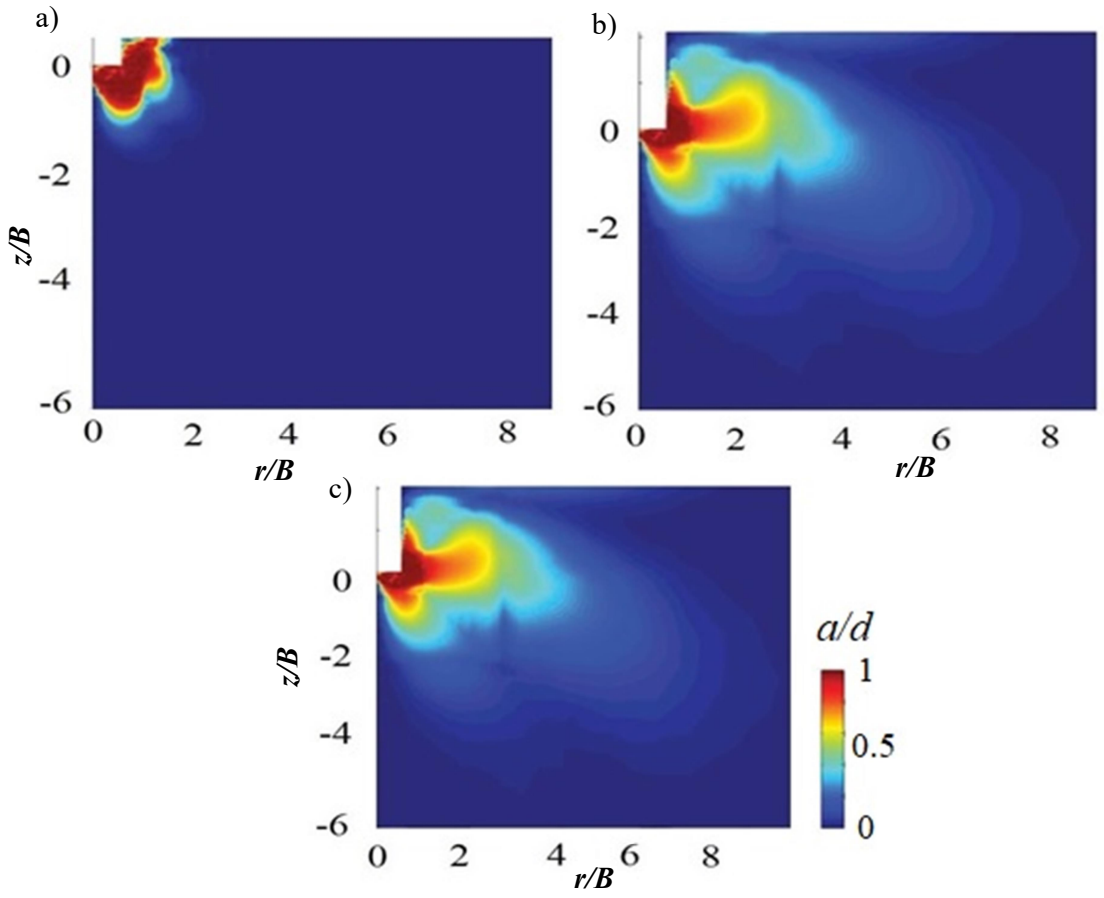

Figure 3.14 Failure patterns for $m = 0$ with a) $H/B = 0.5$, $\alpha_b = 1$, $\alpha_s = 0$; b) $H/B = 2$, $\alpha_b = 1$, $\alpha_s = 0$; and c) $H/B = 2$, $\alpha_b = 1$, $\alpha_s = 1$.

3.3.4 Comparisons with the available solutions

To examine the robustness and the accuracy of the presently used nonlinear optimization process, a comparative study is carried out with the different available literatures and is displayed in Figure 3.15. For homogenous soil (i.e. m = 0), the obtained values of N_c for different H/B with α_b = 1 and α_s = 0 are compared with (i) the Vesic's formulae (1975), (ii) the three-dimensional finite element lower bound solutions computed by Salgado et al. (2004), (iii) the lower bound solutions reported by Khatri and Kumar (2009) on the basis of linearizing the yield surface, (iv) the finite element solution of Hu et al. (1999), and (v) the alternative lower bound solution of Martin and Randolph (2001) by using the method of characteristics along with the usage of the equivalent free surface. It can be noted

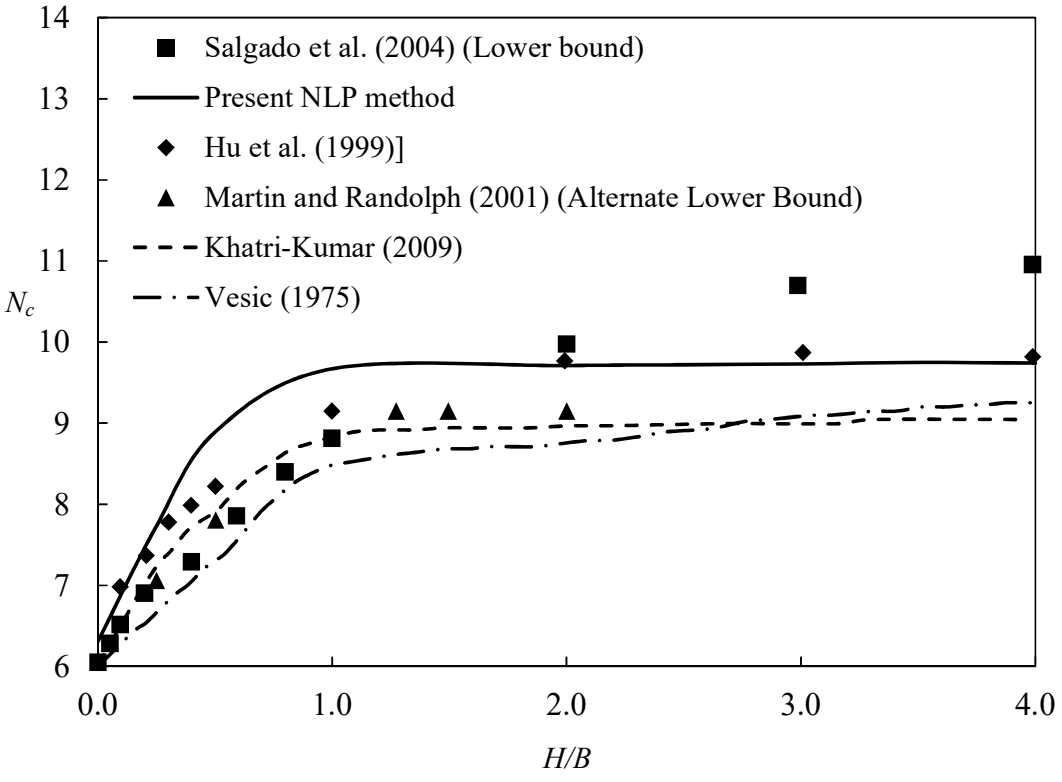

Figure 3.15 A comparison of the variation of N_c with H/B for homogeneous clays (m = 0).

that the present N_c value is higher than all the previously obtained values upto an embedment ratio 2. Beyond H/B = 2, the present solutions are in good agreement with the finite element solutions of Hu et al. (1999). However, solutions provided by Salgado et al. (2004) for $H/B > 2$ is on the higher side from the present one, and the difference is quite noticeable for a higher H/B ratio. It may be worth mentioning that in the work of Salgado et al. (2004), the footing shaft is not modelled. Tables 3.1 and 3.2 depict the comparison of present solutions with the – (i) linear lower bound solutions provided by Khatri and Kumar (2009), (ii) the method of characteristics solutions computed by Houlsby and Martin (2003), and (iii) the alternate lower bound values of Martin (2001). The comparison is made for a smooth pile-shaft surface and different values of m corresponding to two different H/B ratios – 0.5 and 1. The values are compared for both the smooth and rough pile bases. The present solutions are found to be higher than any other solution.

Table 3.1. A comparison of present N_c values with those from literature with α_b = 0, α_s = 0.

m	Present Study	Khatri and Kumar (2009)	Houlsby and Martin (2003)
0	8.55 (9.3)	7.86 (8.58)	6.79 (7.49)
1	8.76 (9.42)	8.36 (8.56)	7.05 (7.47)
2	9.00 (9.44)	8.50 (8.84)	7.15 (7.45)
3	9.04 (9.45)	8.57 (8.84)	7.21 (7.43)
4	9.05 (9.47)	8.61 (8.85)	7.25 (7.44)
5	9.11 (9.47)	8.63 (8.85)	7.27 (7.44)

Note: The values within the parentheses and outside the parentheses represent the magnitude N_c of for H/B = 1 and 0.5, respectively.

Table 3.2. A comparison of present N_c values with those from literature with $\alpha_b = 1$, $\alpha_s = 0$.

m	Present study	Khatri and Kumar (2009)	Houlsby and Martin (2003)	Martin (2001)
0	8.89 (9.67)	7.91 (9.30)	7.05 (7.71)	7.85 (8.84)
1	9.22 (9.83)	8.66 (9.47)	7.60 (7.94)	8.57 (9.29)
2	9.47 (9.84)	8.91 (9.54)	7.80 (7.98)	8.87 (9.29)
3	9.49 (9.85)	9.04 (9.54)	7.91 (7.99)	-
4	9.51 (9.86)	9.12 (9.55)	7.98 (8.00)	-
5	9.56 (9.86)	9.16 (9.55)	8.03 (8.00)	9.08 (9.32)

Note: The values within the parentheses and outside the parentheses represent the magnitude N_c of for H/B = 1 and 0.5, respectively.

3.4 SUMMARY

This chapter showcases a twofold illustration. The first section offers an in-depth representation of an axisymmetric lower bound finite element limit analysis, accompanied by the smoothening operations on yield surfaces, as well as conducting gradient and Hessian based nonlinear optimization. The axisymmetric lower bound limit analysis is carried out by using two-dimensional constant-strain triangular elements and three-dimensional yield criterion. The domain for the axisymmetric problem is planar and does not require a volumetric domain. Each node of the elements are associated with three normal stresses (vertical, radial, and circumferential) and one shear stress. The Mohr-Coulomb and the Tresca yield criterion are used to model the cohesive-frictional and the undrained cohesive soils, respectively. The discontinuities on the yield

surfaces are adequately smoothened (to obtain a C^2 continuous surface) by using the rounding off trigonometric approach in the π-plane and the hyperbolic approximation in the meridian plane. Two controlling parameters are added to the yield function to remove the sharp discontinuities. By adding a log-barrier function, the nonlinear-constrained modified objective function is optimized with the aid of the Hessian-based interior-point method. The barrier parameter reduces in each iteration and approaches zero to provide a statically admissible optimum stress field. Unlike the previous literature, the nonlinear formulation does not require coerced restrictions on circumferential stress.

The second part of this chapter exemplifies the lower-bound solutions for circular piles in undrained and completely saturated clayey soil by using the methodology described in the first section. The solutions are obtained for different (i) roughness conditions along the pile base and the pile shaft and (ii) the rate at which cohesion increases along the depth. It was observed that the magnitude of N_c increases continuously with an increase in H/B up to a certain value beyond which the value of N_c remains almost constant. This study suggests that the roughness of the pile base and shaft affects the magnitudes of bearing capacity; the roughness along the pile shaft plays a crucial role rather than the pile base. The obtained solutions are compared with the existing literature, and it was found that the values are in good agreement with their previous counterpart. The nonlinear optimization technique involved in the process improves the accuracy of the lower-bound solution.